



Article

Drude-Lorentz Model for Optical Properties of Photoexcited Transition Metals under Electron-Phonon Nonequilibrium

Elena Silaeva , Louis Saddier and Jean-Philippe Colombier * 

Laboratoire Hubert Curien, UMR CNRS 5516, UJM, IOGS, Université de Lyon, 42000 Saint-Etienne, France; elena.silaeva@univ-st-etienne.fr (E.S.); louis.saddier@ens-paris-saclay.fr (L.S.)

* Correspondence: jean.philippe.colombier@univ-st-etienne.fr

Abstract: Evaluating the optical properties of matter under the action of ultrafast light is crucial in modeling laser–surface interaction and interpreting laser processing experiments. We report optimized coefficients for the Drude-Lorentz model describing the permittivity of several transition metals (Cr, W, Ti, Fe, Au, and Ni) under electron-phonon nonequilibrium, with electrons heated up to 30,000 K and the lattice staying cold at 300 K. A Basin-hopping algorithm is used to fit the Drude-Lorentz model to the nonequilibrium permittivity calculated using ab initio methods. The fitting coefficients are provided and can be easily inserted into any calculation requiring the optical response of the metals during ultrafast irradiation. Moreover, our results shed light on the electronic structure modifications and the relative contributions of intraband and interband optical transitions at high electron temperatures corresponding to the laser excitation fluence used for surface nanostructuring.

Keywords: Drude-Lorentz model; ab initio; optical properties; ultrafast-laser excitation; transition metals; nanostructuring



Citation: Silaeva, E.; Saddier, L.; Colombier, J.-P. Drude-Lorentz Model for Optical Properties of Photoexcited Transition Metals under Electron-Phonon Nonequilibrium. *Appl. Sci.* **2021**, *11*, 9902. <https://doi.org/10.3390/app11219902>

Academic Editors: Vibhav Bharadwaj and Sanathana Konugolu Venkata Sekar

Received: 29 September 2021
Accepted: 19 October 2021
Published: 23 October 2021

Publisher's Note: MDPI stays neutral with regard to jurisdictional claims in published maps and institutional affiliations.



Copyright: © 2021 by the authors. Licensee MDPI, Basel, Switzerland. This article is an open access article distributed under the terms and conditions of the Creative Commons Attribution (CC BY) license (<https://creativecommons.org/licenses/by/4.0/>).

1. Introduction

Modeling light–metal interaction for ultrafast laser fields remains a challenging issue as the role of transient electronic response in the metal band structure is a dominant factor in optical properties. Intense photoexcitation in the femtosecond range for fluence near the ablation threshold, typically 0.2 J/cm^2 for most of transition metals, forces conduction electrons in metals to move around the lattice ions, enabling photon absorption through an inverse bremsstrahlung process [1]. Beyond this classical view, electrons undergo electron–electron and electron–phonon scattering, resulting in a photon absorption process as well as an internal thermalization [2,3]. Throughout the laser–solid absorption, the electrons are redistributed within the density of states respecting the Pauli exclusion principle. This involves intraband and interband displacements of the electron population, followed by thermalization within the bands [4]. Screening effects determine a subsequent evolution of the bands themselves [5]. The evolution of optical properties relies directly on the transient electronic band structure. The prediction of optical properties thus requires an inaccessible kinetic description, challenging the rationalization of the collective processes. To interpret and predict the optical dynamics in time-dependent ultrashort laser–metal modeling, clarification and simplification of the absorption mechanisms are required. To achieve this, tractable models and simulation approaches capable of describing fast electron dynamics are formulated.

For pure transition metals irradiated in IR–visible range, the absorption length corresponding to the optical skin depth is on a scale of a few tens of nanometers, and the optical properties are determined by the bulk properties. For irradiated quasi-flat and rough surfaces, this strong energy confinement is able to trigger a plethora of surface ultrafast phenomena at the nanoscale [6,7]. The observed material reflectivity and thus the amount of laser energy absorbed in the skin depth is defined by the collective electronic response to the laser field through intraband and interband transitions in sub-bands of the crystal

state [8–12]. The time-resolved complex refractive index of the laser-irradiated surface has been previously reported by a dual-angle reflectometry technique, which was applied to study the optical dynamics of *d*-band electrons in transition metals near the threshold fluence [13–16]. To better determine the refractive index without Fresnel equations, a direct measurement of optical properties has been recently proposed by an ultrafast pump-probe method combining ellipsometry with reflectometry [17,18]. Recent self-reflectivity measurements of femtosecond-laser-heated aluminum and tungsten also confirm the importance of the transient density of states for interpreting the experimental data [19]. Moreover, both time-resolved and integrated optical data showed a strongly increased optical coupling due to the fast variation of the optical properties during irradiation with ultrashort laser pulses.

Fitting these optical properties on a relatively large spectrum is of great interest for spectroscopy, plasmonics, nanophotonics, and optical engineering, which requires dispersion models, such as Drude, Drude-Lorentz, Critical Points, or Partial-Fraction [20–22]. The goal of the present work is to propose a straightforward Drude-Lorentz model with electron-phonon nonequilibrium parameters that ultimately aims at being implemented into numerical models as Maxwell solvers. Our approach provides fitting values of optical properties during the nonequilibrium state lasting a few picoseconds when the lattice temperature remains undisturbed at 300 K, modifying the material primary response to the laser irradiation. A “hot” electron temperature range of 10,000–30,000 K was considered to obtain a non-negligible effect on permittivity and, at the same time, to work in the limits of material stability [23]. Such temperatures are expected for the typical laser irradiation parameters: pulse duration 10–100 fs, fluence 0.1–0.2 J/cm² and wavelength 800 nm [4,19]. We assume that the lattice is at room temperature for generality and larger applicability to different nonequilibrium conditions even though an increase of 100–300 K can be expected within 100 fs. Such an increase is insignificant in the given study since the lattice temperature stays well below the melting threshold.

The nonequilibrium data were obtained using *ab initio* molecular dynamics and the Kubo-Greenwood formalism [14,24]. These calculations, combined with Kramers-Kronig relations, give access to the complex optical permittivities of the considered metals for several electron temperatures from 300 K to 30,000 K. They serve as reference points for the fitting process for real and imaginary parts of the permittivities, optimizing parameters such as oscillator and collision frequencies. (In their attempt to describe the interaction between atoms and electric fields in classical terms, Lorentz proposed that electrons are bound to the ions by a force that behaves as a spring, according to Hooke’s Law. In the so-called Lorentz oscillator model, the applied electric field interacting with the electron charge, causes stretching or compression of the spring, which sets the electron into oscillating motion.)

2. Methods

First, *ab initio* calculations of optical permittivity have been performed for different transition metals (Cr, W, Ti, Fe, Au, and Ni) at different electron temperatures up to 30,000 K using ABINIT software [25]. The electronic structure (density of states, band filling, electron distribution) were calculated using a finite-temperature density functional theory with appropriate exchange-correlation functionals (GGA for Cr, W, Ti, Fe, and Ni and LDA for Au) and projector-augmented wave atomic data to consider nuclei and core electrons effects. The finite electronic temperature T_e is taken into account by considering a Fermi-Dirac distribution function applied to the Kohn-Sham eigenstates, thus describing a T_e -dependent electronic structure as a result of self-consistent calculation. The quantum molecular dynamic simulation was performed at an ionic temperature of 300 K to account for electron-phonon interaction in optical properties. Then we used a Kubo-Greenwood formalism to describe the possible electronic transitions and Kramers-Kronig relation to finally calculate the permittivity. The high electron temperature is considered to reproduce the transient distribution of photoexcited electrons at the laser pulse fluences used for nanostructuring. A detailed description of these calculations can be found in our previous work [24] with some additional information for Au in Ref. [5].

Then, the Drude-Lorentz model was fitted to the ab initio permittivity with the aim of providing a simple and convenient way to interpret and apply the calculated data. The Drude-Lorentz model is often used for the parametrization of optical constants of metals [20] with the complex permittivity dispersion describing the free electrons (intraband transitions) and bound electrons (interband transitions):

$$\epsilon(\omega) = \epsilon(\omega)^{(f)} + \epsilon(\omega)^{(b)}. \quad (1)$$

The intraband contribution $\epsilon(\omega)^{(f)}$ is described by the free-electron Drude model:

$$\epsilon(\omega)^{(f)} = 1 - \frac{f_0 \omega_p^2}{\omega(\omega - i\Gamma_0)}, \quad (2)$$

where ω_p is the plasma frequency, f_0 is the free-electron oscillator strength, and Γ_0 is the damping constant related to the electron collision frequency. The interband contribution $\epsilon(\omega)^{(b)}$ follows the Lorentz model:

$$\epsilon(\omega)^{(b)} = \sum_{j=1}^k \frac{f_j \omega_p^2}{\omega_j^2 - \omega^2 - i\omega\Gamma_j}, \quad (3)$$

which describes k interband transitions with frequency ω_j , oscillator strength f_j , and lifetime $1/\Gamma_j$.

To fit the Drude-Lorentz model to the ab initio data, the Basin-hopping optimization method was used. The Basin-hopping algorithm was designed to mimic the energy minimization of clusters of atoms and thus is suitable for our case where the Drude-Lorentz oscillators have similar energy landscapes [26]. The difference between the model and the data was minimized based on the objective function χ^2 :

$$\chi^2 = \sum_{i=1}^N \left[\left| \frac{\epsilon_1(\omega_i) - \epsilon_1^{data}(\omega_i)}{\epsilon_1^{data}(\omega_i)} \right| + \left| \frac{\epsilon_2(\omega_i) - \epsilon_2^{data}(\omega_i)}{\epsilon_2^{data}(\omega_i)} \right| \right]^2, \quad (4)$$

where the sum runs over all N data points, and ϵ_1 and ϵ_2 are the real and imaginary parts of the permittivity $\epsilon = \epsilon_1 + i\epsilon_2$. Note that the relative permittivity is considered everywhere. A reduced objective function $\chi_r^2 = \chi^2/N$ was also calculated and presented below. A value of χ_r^2 less than unity is expected for a good fit. A Python code implementing the data fitting is provided in the Supplementary Materials.

During the optimization procedure, we fixed $k = 4$ in Equation (3). The preliminary analysis showed that such a number of interband terms was sufficient for all considered metals and electron temperatures. For significant results and faster convergence, we also set the constraints on the optimization parameters guided by the physical sense and the values reported in [20]. The plasma frequency in Equations (2) and (3) is related to the free-electron density n_e by the equation $\omega_p = \sqrt{\frac{n_e e^2}{m_e \epsilon_0}}$. Note that the free-electron oscillator strength $f_0 = \frac{m_e}{m_e^*}$ is often included in the plasma frequency via the electron effective mass m_e^* . The free-electron density depends on the electron temperature T_e and was estimated from ab initio calculations using the procedure described in Ref. [5]. Both n_e and ω_p are reported in Table 1 at different electron temperatures.

3. Results

The Drude-Lorentz model is mostly used to fit the experimental data for different metals and frequency intervals [20,27,28]. Thus, we first made sure that the proposed algorithm can correctly fit the experimentally measured permittivities. The optimal values for the model parameters obtained for the experimental data tabulated in the *Handbook on Optical Constants of Metals* (Adachi, 2012) [29] are given in Table 2 (Γ_j and ω_j are in eV). The model was fitted in the 0.05–6 eV range with $k = 4$ interband oscillators and the plasma

frequencies given in Table 1 at 300 K. Figure 1 shows a general good agreement between our model and experimental data for all considered metals.

Table 1. Free-electron densities n_e and plasma frequencies ω_p for different metals at different electron temperatures T_e .

Metal	T_e (K)	n_e (10^{23} cm^{-3})	$\hbar\omega_p$ (eV)
Cr	300	1.67	15.17
	10,000	1.67	15.17
	25,000	1.67	15.17
W	300	1.40	13.88
	10,000	1.40	13.88
	25000	1.52	14.50
Ti	300	0.79	10.45
	10,000	0.79	10.45
	25,000	0.85	10.82
Fe	300	1.11	12.36
	15,000	1.28	13.28
	30,000	1.45	14.14
Au	300	1.42	13.98
	10,000	1.47	14.26
	25,000	1.65	15.10
Ni	300	1.28	13.28
	10,000	1.55	14.63
	25,000	1.83	15.87

Table 2. Drude-Lorentz model coefficients used for fitting the experimental data.

Coefficient	Cr	W	Ti	Fe	Au	Ni
f_0	0.100	0.182	0.067	0.103	0.144	0.139
Γ_0	0.042	0.053	0.036	0.016	0.001	0.038
f_1	0.198	0.014	0.082	0.652	0.192	0.107
Γ_1	2.134	0.250	0.648	2.994	0.125	0.765
ω_1	0.863	0.973	0.676	0.469	0.010	0.415
f_2	0.398	0.019	0.557	0.015	0.026	0.448
Γ_2	2.158	0.407	2.472	0.566	0.779	3.007
ω_2	1.877	3.490	1.692	1.561	3.003	1.439
f_3	0.036	2.370	0.066	0.193	0.168	0.276
Γ_3	0.608	9.340	1.509	1.701	2.136	2.311
ω_3	2.353	3.750	5.636	2.564	4.134	4.675
f_4	0.927	0.426	1.266	1.170	0.744	0.673
Γ_4	9.999	1.140	9.450	9.780	4.685	1.489
ω_4	9.831	5.338	8.871	8.023	7.586	9.439
χ_r^2	0.097	0.206	0.461	0.028	0.518	0.013

The results of ab initio calculations and the optimized Drude-Lorentz model at different electron temperatures are shown in Figure 2 for Cr, W, and Ti and in Figure 3 for Fe, Au, and Ni, with the values of the optimization parameters given in Tables 3 and 4, respectively. The fitting range 0.05–6 eV was chosen to correspond to the photon energies used for laser-induced nanostructuring. Figures 2 and 3 reveal that the proposed algorithm performed well for most of the cases, especially to reproduce the imaginary part behaviour. The discrepancies appear for the real part of Au permittivity at 300 K and 10,000 K as the global-optimization method is less well-suited to reproduce strong local oscillations. This is also related to the fact that density functional theory calculations using the LDA potential cannot properly reproduce bound electrons and thus are not accurate for Au. However, it is interesting to note that at a higher electron temperature, the Au permittivity becomes

smoother, and the Drude-Lorentz fitting model proves to be more efficient. The same statement is true for most of the metals excited at high T_e . For higher electron temperatures, the Fermi-Dirac distribution of electrons becomes less abrupt around the Fermi level E_f , spreading the allowed optical transitions on a larger energy domain. This softens the peak effects of the density of states (DOS), leading to a smoother permittivity describing the optical transitions of the smeared electrons. Electron distribution smearing intrinsically decreases the error in the calculation of optical transitions around the sharp features of the electron DOS within the d band for transition metals.

Remarkably, the ab initio permittivity is more accurate at high electron temperatures and probably less dependent on the inherent variation of the experimental material preparation process. At a high T_e , the electrons occupy high-energy delocalized states, the electron density becomes more homogeneous compared to that at zero T_e , and the LDA potential, derived from the exchange-correlation functional of a homogeneous electron gas, becomes more accurate [30]. As a result, although the experimental and ab initio permittivities disagree for some metals and energy ranges at 300 K (after comparing Figure 1 and Figures 2 and 3), that does not invalidate the calculations at higher T_e . The procedure to measure the optical constants is very sensitive to the experimental conditions, quality of the metal surface, and data extraction methods that may be at the origin of the disagreement at 300 K. Some other experimental data sets reported in the literature agree well with ab initio calculations [24]. Additionally, the ab initio permittivity describes an ideal case of a pure metal and perfect illumination conditions that are hard to achieve experimentally.

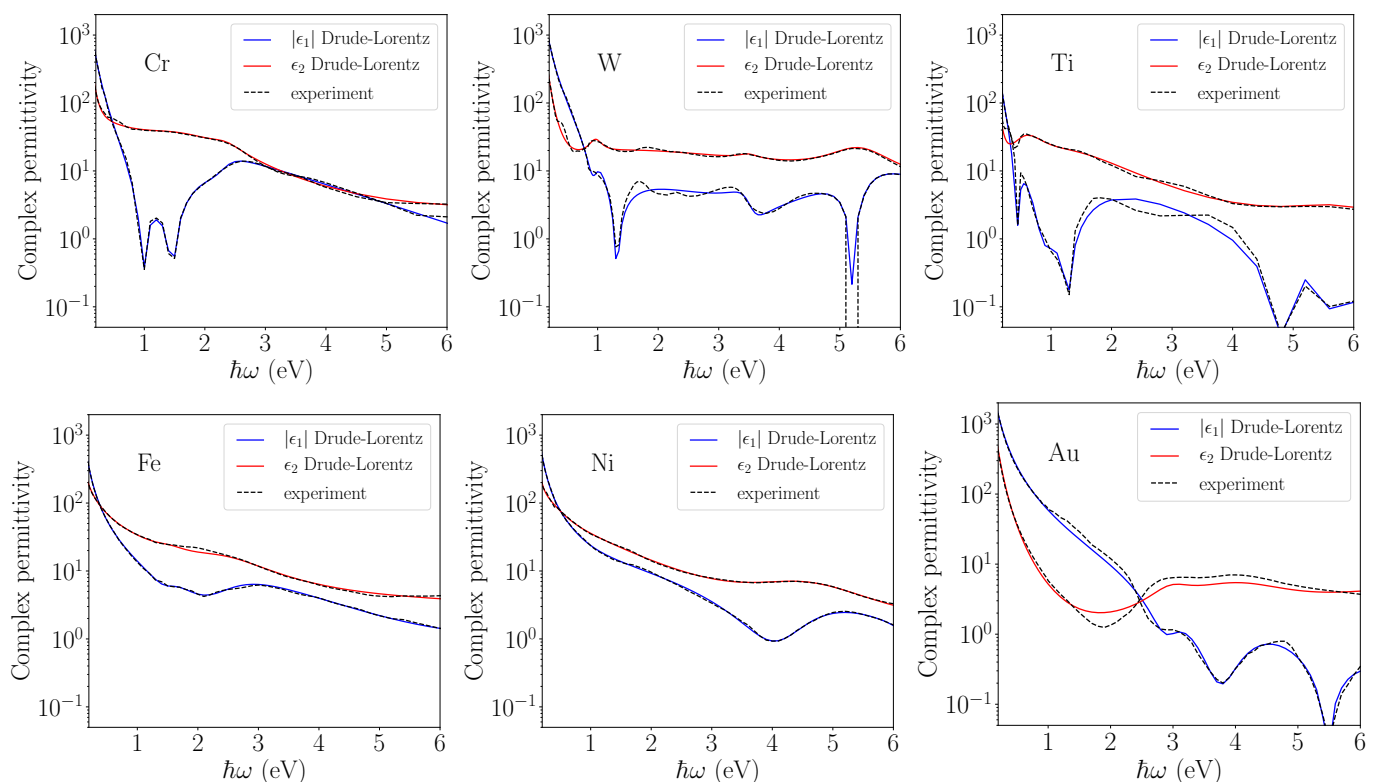


Figure 1. Drude–Lorentz fit of experimental permittivity at 300 K reported in the *Handbook on Optical Constants of Metals* (Adachi, 2012) [29]. The real ϵ_1 and imaginary ϵ_2 parts of the permittivity are shown. An electron–phonon equilibrium is considered.

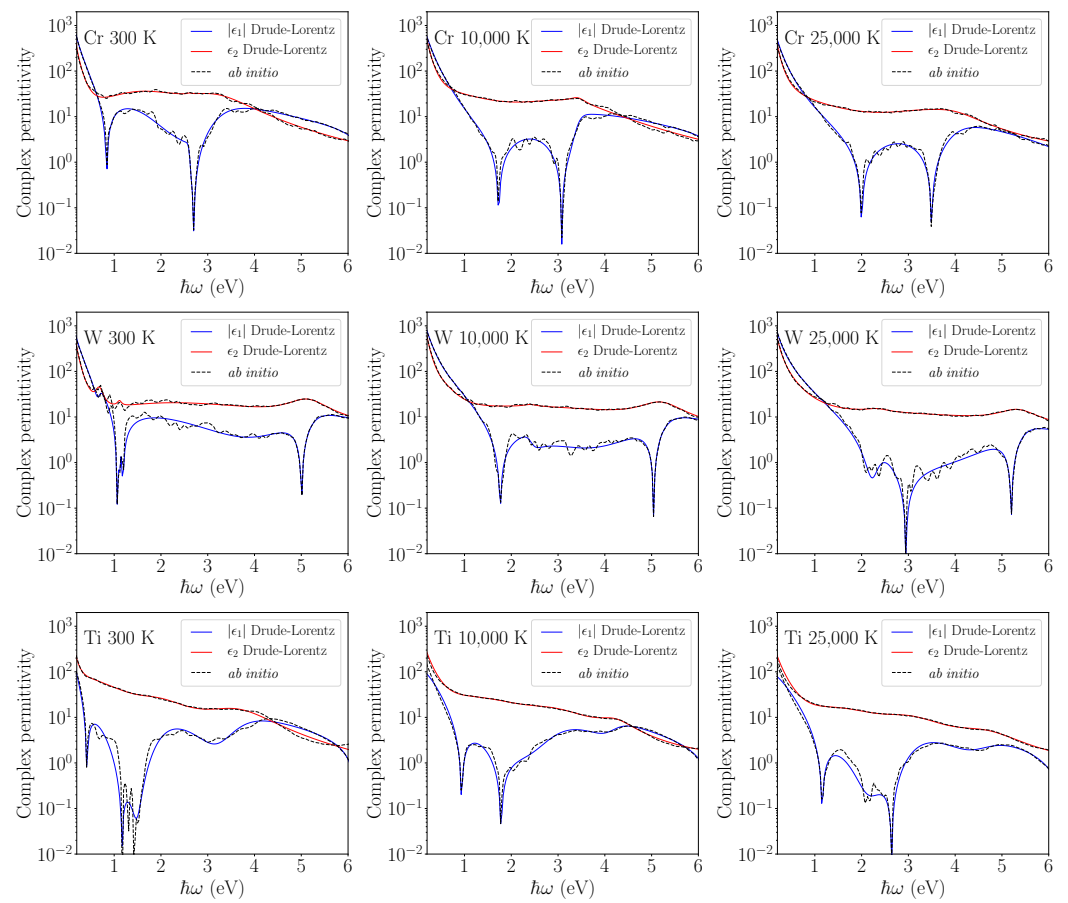


Figure 2. Drude–Lorentz fit of permittivity calculated using ab initio methods for Cr, W, and Ti. The real ϵ_1 and imaginary ϵ_2 parts of permittivity are shown at different electron temperatures corresponding to different levels of electron–phonon nonequilibrium.

Table 3. Drude–Lorentz model fitting coefficients for the permittivity calculated using ab initio methods for Cr, W, and Ti.

Coefficient	Cr			W			Ti		
	300 K	10,000 K	25,000 K	300 K	10,000 K	25,000 K	300 K	10,000 K	25,000 K
f_0	0.132	0.168	0.133	0.156	0.249	0.185	0.115	0.241	0.199
Γ_0	0.110	0.154	0.138	0.120	0.137	0.107	0.177	0.417	0.447
f_1	0.567	0.312	0.388	0.015	0.052	0.131	0.694	0.783	0.377
Γ_1	2.382	2.855	4.571	0.171	0.840	1.040	1.932	2.592	2.188
ω_1	1.935	1.411	1.578	0.686	0.652	0.325	0.936	1.751	1.823
f_2	0.002	0.569	0.204	0.003	0.008	0.015	0.306	0.374	0.274
Γ_2	0.100	2.437	2.105	0.100	0.333	0.579	1.363	1.760	1.685
ω_2	2.608	3.302	3.446	1.114	2.412	2.343	2.062	3.024	3.126
f_3	0.471	0.038	0.121	2.038	1.837	1.860	0.602	0.140	0.189
Γ_3	1.640	0.396	1.342	6.709	7.195	9.992	1.626	0.878	1.666
ω_3	3.241	3.423	3.976	3.668	3.933	4.813	3.689	4.223	4.690
f_4	0.128	0.153	0.495	0.376	0.348	0.175	0.370	0.419	0.544
Γ_4	0.001	0.001	1.512	0.961	1.023	0.952	0.001	0.212	0.458
ω_4	6.773	7.187	9.614	5.141	5.209	5.347	6.882	7.275	8.058
χ_r^2	0.299	0.521	0.320	0.587	0.301	0.588	0.878	0.436	0.691

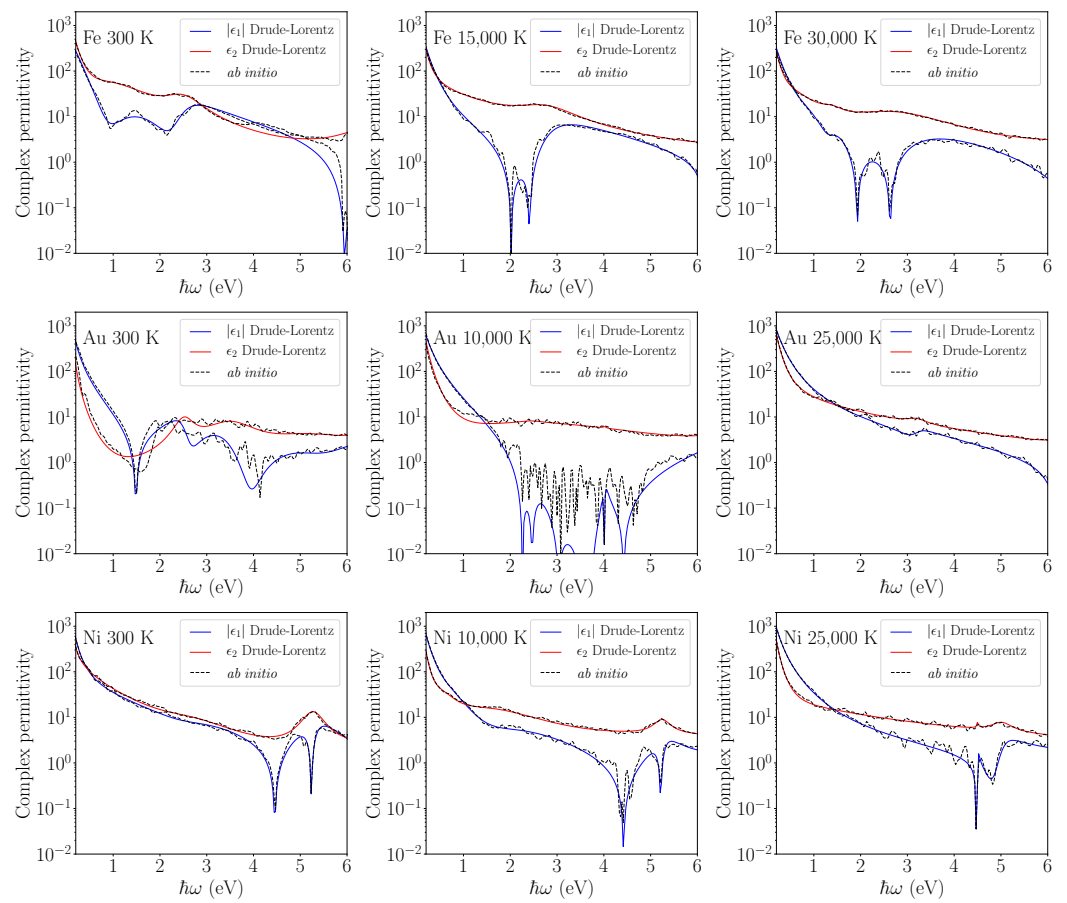


Figure 3. Drude–Lorentz fit of permittivity calculated using ab initio methods for Fe, Au, and Ni. The real ϵ_1 and imaginary ϵ_2 parts of permittivity are shown at different electron temperatures corresponding to different levels of the electron–phonon nonequilibrium.

Table 4. Drude-Lorentz model fitting coefficients for the permittivity calculated using ab initio methods for Fe, Au and Ni.

Coefficient	Fe			Au			Ni		
	300 K	15,000 K	30,000 K	300 K	10,000 K	25,000 K	300 K	10,000 K	25,000 K
f_0	0.234	0.134	0.110	0.099	0.184	0.235	0.165	0.149	0.191
Γ_0	0.254	0.141	0.148	0.060	0.146	0.150	0.069	0.077	0.100
f_1	0.639	0.664	0.088	0.045	0.006	0.753	0.499	0.037	0.762
Γ_1	1.895	4.302	1.167	0.461	0.618	7.133	2.009	0.707	8.704
ω_1	1.280	1.325	0.770	2.530	2.457	2.069	0.628	0.638	2.754
f_2	0.280	0.211	0.020	0.152	0.651	0.013	0.103	0.278	0.001
Γ_2	0.904	1.399	0.587	1.263	6.075	0.491	1.820	2.648	0.037
ω_2	2.512	2.821	1.401	3.545	3.738	3.207	2.797	1.967	4.502
f_3	0.026	0.013	0.414	0.146	0.001	0.006	0.180	0.046	0.030
Γ_3	0.754	0.006	2.677	2.107	0.072	0.300	0.532	0.404	0.513
ω_3	6.131	6.352	2.970	5.261	4.016	6.251	5.277	5.250	5.021
f_4	0.721	1.570	1.107	0.512	0.368	0.657	0.313	0.686	0.255
Γ_4	2.311	7.397	8.961	1.493	1.194	2.158	1.458	7.070	8.779
ω_4	7.492	12.540	10.025	7.431	7.470	10.654	7.297	6.737	7.250
χ^2_T	1.621	0.688	0.405	3.486	4.930	0.146	0.392	0.919	0.565

To understand other effects of a high electron temperature on permittivity, we analyzed the intraband and interband contributions separately. The contribution of intraband transitions to the permittivity generally increases with electron temperature, as shown in Figure 4. The high electron temperature also influences the relative strength of the interband transitions and shifts the interband transition energy, as can be seen from the evolution

of the optimization parameters f_j, ω_j, Γ_j with temperatures from Tables 3 and 4. This is also seen from Figure 5, where the contributions to the imaginary part of permittivity from different oscillators (order 0 to 4) are plotted separately. Different terms can thus be easily identified. The intraband term (the oscillator of 0th order) is high in the infrared range below 1 eV. While the maximum is at zero photon energy limit, the intraband contribution decreases quickly at higher photon energies. The interband terms have a Lorentzian shape with different heights, widths, and locations. These features are modeled by f_j, ω_j , and Γ_j values with higher order corresponding to a higher central frequency ω_j . For some cases, the frequency of the fourth-order oscillator is higher than the chosen range and thus does not appear on the graph. Note that for some cases, Γ_j reaches the set constraint of 0.001 and thus does not provide any physical meaning. It happens, however, either for the fourth oscillator or for other insignificant oscillators (such as a tiny second oscillator for Cr). Additionally, the first-order oscillator is sometimes similar in behavior to the zero-order oscillator, as obtained by the optimization procedure (for example, for W, at 25,000 K) with both zero and first orders exhibiting a continuous decrease with $\hbar\omega$, which is characteristic of an intraband trend. In this case, the intraband contribution was considered as a sum of the zero- and first-order oscillators.

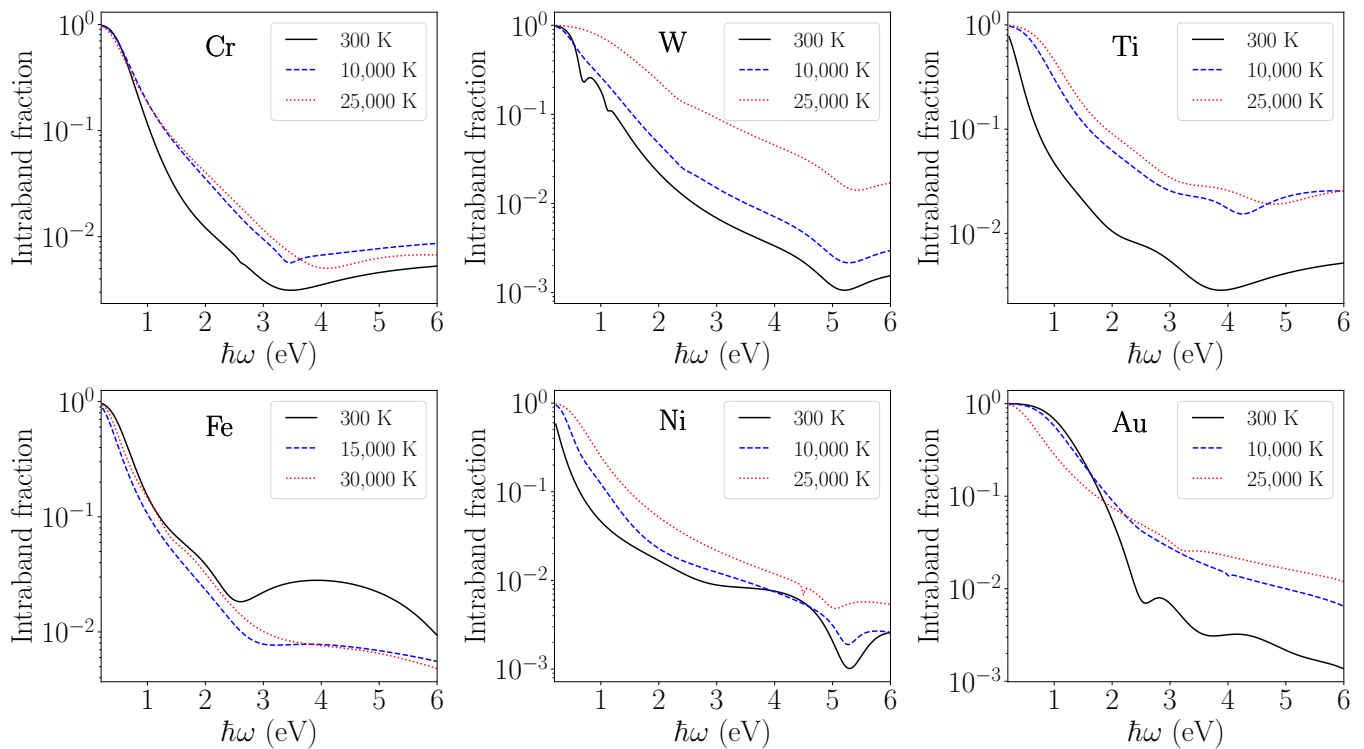


Figure 4. Fraction of the intraband contribution to the imaginary part of permittivity at different electron temperatures for the six transition metals.

It is generally believed that for a strong laser excitation, equivalent to a high electron temperature in our case, the interband oscillators change their relative strength f_j (becoming stronger or weaker) and width Γ_j , whereas the central frequency ω_j remains constant [16]. We can see, however, in Figure 5 that the position of the oscillator maxima changes too. For example, the third-order oscillator of Ti shifts from about 3.7 eV at 300 K to 4.7 eV at 25,000 K. Such shifts reflect the changes of the DOS of the transition metals at high excitation levels [5] and are discussed in more detail in the following section.

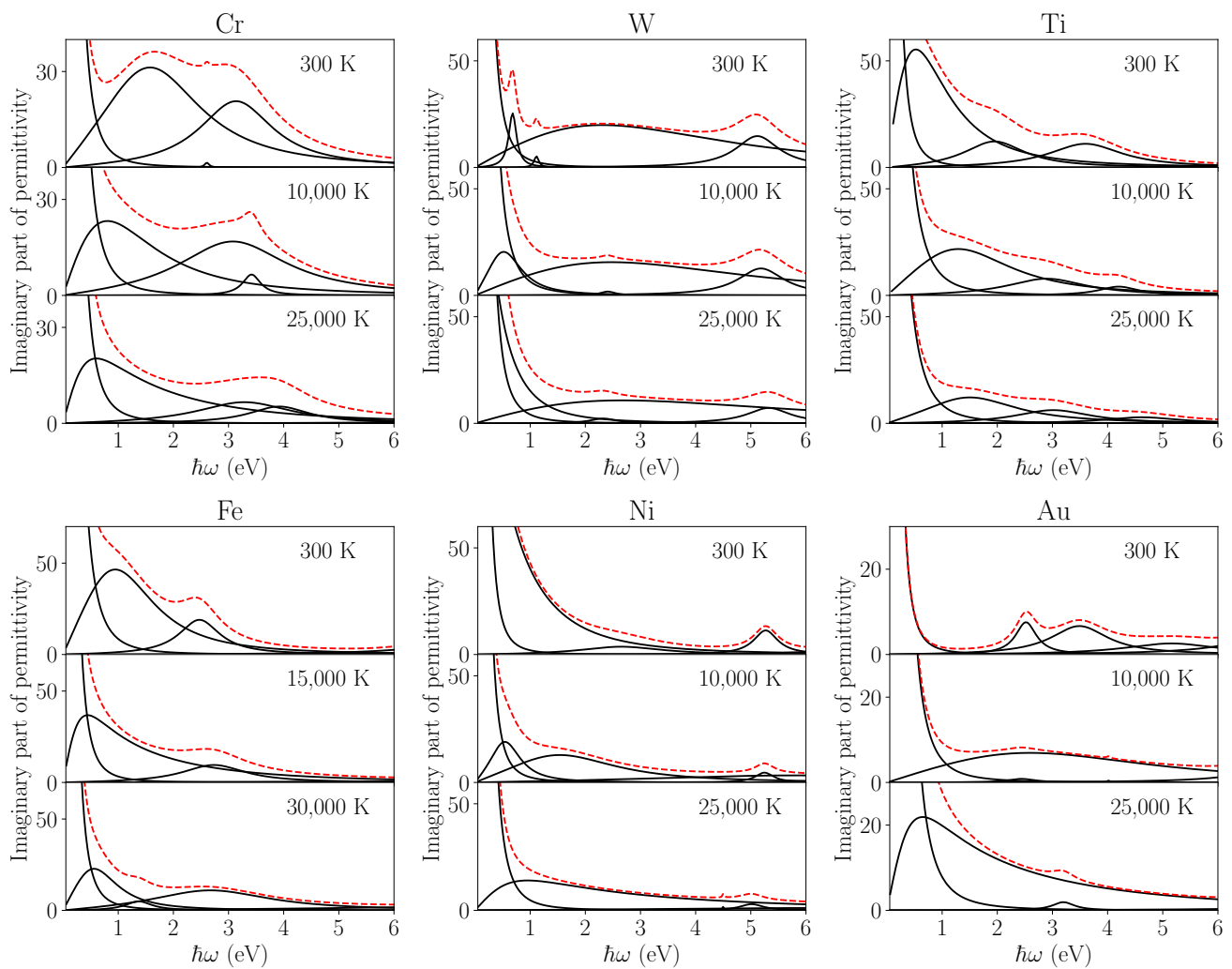


Figure 5. Imaginary part of the permittivity (dashed line) and contributions of each Drude–Lorentz term (solid lines) at different electron temperatures for the six transition metals. Drude term (0-order oscillator) reaches maximum at zero frequency and is followed by Lorentzians describing the 1st-, 2nd-, 3rd and 4th-order oscillators with a higher order corresponding to a higher central frequency. The 4th-order oscillator appears only for W, but for other metals, it is out of the shown frequency range.

4. Discussion

The optical properties of transition metals are largely defined by the features of their electronic structure. Contrary to simple metals, such as Al, Mg, or Zn, transition metals are characterized by the presence of *d*-bands that translate into a high-density *d*-block in the DOS [5]. The *d*-block represents highly localized electron states filled with bound-like electrons. The metallic elements used in this study are representative to capture the electronic and optical characteristics for a broad variety of transition metals. During the laser excitation, the electrons thermalize and redistribute almost instantly (on the femtosecond time scale) within the DOS [4,31]. The *d*-block is affected by laser-induced Fermi smearing of electrons extending the energy range available for optical transitions and thus strongly impacting the permittivity. Particularly, the position of the *d*-block relative to the Fermi level defines the strength of the interband component of the permittivity as a function of the photon energy. The *d*-block also serves as a reservoir for populating upper free-like states, and its electronic filling degree thus defines the direct transitions within and from the *d*-states. The other part of the DOS corresponds to spatially and energetically delocalized *sp*-states and mainly defines the intraband component.

In Au, the *d*-block is completely filled and separated from the Fermi level by about 2 eV. This favors significant interband transitions from the *d*-band to the *sp*-band in the visible range for photon energy higher than 2 eV with intra-*sp*-band transitions prevailing below 2 eV. This is almost the case for Ni as well, with the Fermi level being close to the top of the *d*-block and intraband transitions dominating in the infrared range. For Cr, W, Ti, and Fe, the *d*-states are partially filled, fostering interband contribution for a wide range of photon energies with the intraband transitions inside the *d*-band at low photon energies. The estimated relative contribution of the intraband process to the total optical transitions is presented in Figure 4. As expected, for photons in the infrared and near-infrared region at $\hbar\omega < 1$ eV, intraband transitions are largely dominant.

For higher photon energies $\hbar\omega > 1$ eV, interband transitions dominate over all spectra for all metals, although at a higher electron temperature, the intraband role in the optical response is strengthened. For Au and Ni, a high electron temperature leads to the loss of the localized *d*-electrons and the increase in the density of delocalized *sp*-electrons that results in the shift of the *d*-block towards low energies. For Cr, Fe, Ti, and W, the effect of electronic heating induces an inverse electron flow, and the *d*-block shifts towards higher energies. The modification of the DOS manifested mainly by the shift of the *d*-block impacts the interband contribution of the permittivity with a large effect related to the shift of the oscillator positions (Figure 5). The Fermi–Dirac smearing at a high electron temperature significantly populates *sp*-states while decreasing the *d*-band filling, leading to the increase in the intraband fraction, as shown in Figure 4. The opposite behavior of Fe is remarkable as due to the DOS modification, the *d*-block becomes completely filled upon electron heating, fostering interband transitions under a strong nonequilibrium. The loss or gain of electronic localization and its effect on the DOS can be graphically visualized in our previous paper [24].

The above observations underline the need to consider oscillator shifts in a nonequilibrium Drude–Lorentz model, as featured in Figure 5. It disentangles the contributions from different oscillators to the permittivity as a function of the excitation level. The general trend that emerges is that relative contributions of the highest-order oscillators flatten towards being almost negligible at a high T_e . Moreover, the central frequency of the first oscillator shifts toward low energy, indicating a progressive interband-to-intraband conversion. A linear extrapolation of the fitting coefficients is possible for “hot” temperatures covering the experimental range of 5000–50,000 K (according to our tests). In this case, the Drude–Lorentz model could become an effective tool to describe the optical response of photoexcited transition metals.

5. Conclusions

To summarize, a Drude–Lorentz model coefficients describing the permittivity dispersion of laser-excited transition metals are proposed. A simple Basin-hopping optimization algorithm was applied to the data obtained from the ab initio calculations at a finite electron temperature mimicking the transient ultrafast-laser excitation conditions when the electrons and the lattice are out of the equilibrium. These coefficients can be easily used in electromagnetic field solvers where the dispersion model of the laser-excited transition metal is needed, for example, in direct laser-surface energy coupling prediction or even in diffraction gratings, photonic crystals, and resonator band-gap analysis. We also showed that the permittivity is strongly affected by the electron redistribution and changes in the density of states induced by the increase in electron temperature. The energy of the interband transitions is shifted as collective electron motion occurs via many-body effects and the interband contribution to the total permittivity decreases. Our results have far-reaching effects as they propose a route for achieving a high control of transient energy deposition under ultrashort laser irradiation in the regime of fluence corresponding to nanostructuring.

Supplementary Materials: Supplementary data to this article (Python code, tabulated experimental, and ab initio data) can be found online at <https://www.mdpi.com/article/10.3390/app11219902/s1>.

Author Contributions: Conceptualization, J.-P.C.; methodology, E.S. and J.-P.C.; software, E.S. and L.S.; validation, E.S., L.S. and J.-P.C.; formal analysis, E.S. and J.-P.C.; investigation, E.S. and L.S.; resources, L.S.; data curation, E.S.; writing—original draft preparation, E.S.; writing—review and editing, J.-P.C.; visualization, E.S. and L.S.; supervision, J.-P.C.; project administration, J.-P.C.; funding acquisition, E.S. and J.-P.C. All authors have read and agreed to the published version of the manuscript.

Funding: This work was funded by the LABEX MANUTECH-SISE (ANR-10-LABX-0075) of the Université de Lyon, within the program “Investissements d’Avenir” (ANR-11-IDEX-0007) and by the IDEXLYON (ANR-16-IDEX-0005) within the program “Impulsion” operated by the French National Research Agency (ANR).

Institutional Review Board Statement: Not applicable.

Informed Consent Statement: Not applicable.

Data Availability Statement: The data presented in this study are available in the Supplementary Materials.

Acknowledgments: Part of the numerical calculations has been performed using computer resources from GENCI, project gen7041.

Conflicts of Interest: The authors declare no conflict of interest. The funders had no role in the design of the study; in the collection, analyses, or interpretation of data; in the writing of the manuscript, or in the decision to publish the results.

References

1. Seely, J.F.; Harris, E.G. Heating of a Plasma by Multiphoton Inverse Bremsstrahlung. *Phys. Rev. A* **1973**, *7*, 1064–1067. [[CrossRef](#)]
2. Rethfeld, B.; Kaiser, A.; Vicanek, M.; Simon, G. Ultrafast dynamics of nonequilibrium electrons in metals under femtosecond laser irradiation. *Phys. Rev. B* **2002**, *65*, 214303. [[CrossRef](#)]
3. Mueller, B.; Rethfeld, B. Relaxation dynamics in laser-excited metals under nonequilibrium conditions. *Phys. Rev. B* **2013**, *87*, 035139. [[CrossRef](#)]
4. Silaeva, E.; Bévilion, E.; Stoian, R.; Colombier, J.P. Ultrafast electron dynamics and orbital-dependent thermalization in photoexcited metals. *Phys. Rev. B* **2018**, *98*, 094306. [[CrossRef](#)]
5. Bévilion, E.; Colombier, J.P.; Recoules, V.; Stoian, R. Free-electron properties of metals under ultrafast laser-induced electron-phonon nonequilibrium: A first-principles study. *Phys. Rev. B* **2014**, *89*, 115117. [[CrossRef](#)]
6. Bonse, J.; Zergioti, I.; Delaporte, P.; Scarisoreanu, N.D. Special issue on: Laser and plasma processing for advanced applications in material science (E-MRS 2015 Spring Meeting Symposium) Preface. *Appl. Surf. Sci.* **2016**, *374*, 1. [[CrossRef](#)]
7. Stoian, R.; Colombier, J.P. Advances in ultrafast laser structuring of materials at the nanoscale. *Nanophotonics* **2020**, *9*, 4665–4688. [[CrossRef](#)]
8. Fisher, D.; Fraenkel, M.; Henis, Z.; Moshe, E.; Eliezer, S. Interband and intraband (Drude) contributions to femtosecond laser absorption in aluminum. *Phys. Rev. E* **2001**, *65*, 016409. [[CrossRef](#)]
9. Hopkins, P.E.; Duda, J.C.; Salaway, R.N.; Smoyer, J.L.; Norris, P.M. Effects of intra- and interband transitions on electron-phonon coupling and electron heat capacity after short-pulsed laser heating. *Nanoscale Microscale Thermophys. Eng.* **2008**, *12*, 320–333. [[CrossRef](#)]
10. Colombier, J.P.; Combis, P.; Audouard, E.; Stoian, R. Transient optical response of ultrafast nonequilibrium excited metals: Effects of electron-electron contribution to collisional absorption. *Phys. Rev. E* **2008**, *77*, 036409. [[CrossRef](#)] [[PubMed](#)]
11. Kirkwood, S.E.; Tsui, Y.Y.; Fedosejevs, R.; Brantov, A.V.; Bychenkov, V.Y. Experimental and theoretical study of absorption of femtosecond laser pulses in interaction with solid copper targets. *Phys. Rev. B* **2009**, *79*, 144120. [[CrossRef](#)]
12. Loboda, P.; Smirnov, N.; Shadrin, A.; Karlykhanov, N. Simulation of absorption of femtosecond laser pulses in solid-density copper. *High Energy Density Phys.* **2011**, *7*, 361–370. [[CrossRef](#)]
13. Zhang, H.; Li, C.; Bevilion, E.; Cheng, G.; Colombier, J.P.; Stoian, R. Ultrafast destructuring of laser-irradiated tungsten: Thermal or nonthermal process. *Phys. Rev. B* **2016**, *94*, 224103. [[CrossRef](#)]
14. Bévilion, E.; Colombier, J.P.; Recoules, V.; Zhang, H.; Li, C.; Stoian, R. Ultrafast switching of surface plasmonic conditions in nonplasmonic metals. *Phys. Rev. B* **2016**, *93*, 165416. [[CrossRef](#)]
15. Rapp, S.; Kaiser, M.; Schmidt, M.; Huber, H.P. Ultrafast pump-probe ellipsometry setup for the measurement of transient optical properties during laser ablation. *Opt. Express* **2016**, *24*, 17572–17592. [[CrossRef](#)] [[PubMed](#)]
16. Winter, J.; Rapp, S.; Schmidt, M.; Huber, H.P. Ultrafast laser processing of copper: A comparative study of experimental and simulated transient optical properties. *Appl. Surf. Sci.* **2017**, *417*, 2–15. [[CrossRef](#)]

17. Pflug, T.; Wang, J.; Olbrich, M.; Frank, M.; Horn, A. Case study on the dynamics of ultrafast laser heating and ablation of gold thin films by ultrafast pump-probe reflectometry and ellipsometry. *Appl. Phys. A* **2018**, *124*, 1–7.
18. Winter, J.; Rapp, S.; Spellaugue, M.; Eulenkamp, C.; Schmidt, M.; Huber, H.P. Ultrafast pump-probe ellipsometry and microscopy reveal the surface dynamics of femtosecond laser ablation of aluminium and stainless steel. *Appl. Surf. Sci.* **2020**, *511*, 145514. [[CrossRef](#)]
19. Genieys, T.; Sentis, M.; Utéza, O. Investigation of ultrashort laser excitation of aluminum and tungsten by reflectivity measurements. *Appl. Phys. A* **2020**, *126*, 1–14. [[CrossRef](#)]
20. Rakić, A.D.; Djurišić, A.B.; Elazar, J.M.; Majewski, M.L. Optical properties of metallic films for vertical-cavity optoelectronic devices. *Appl. Opt.* **1998**, *37*, 5271–5283. [[CrossRef](#)]
21. Vial, A.; Laroche, T. Description of dispersion properties of metals by means of the critical points model and application to the study of resonant structures using the FDTD method. *J. Phys. D Appl. Phys.* **2007**, *40*, 7152. [[CrossRef](#)]
22. Han, L.; Zhou, D.; Li, K.; Li, X.; Huang, W.P. A rational-fraction dispersion model for efficient simulation of dispersive material in FDTD method. *J. Light. Technol.* **2012**, *30*, 2216–2225. [[CrossRef](#)]
23. Ben-Mahfoud, L.; Silaeva, E.P.; Stoian, R.; Colombier, J.P. Structural instability of transition metals upon ultrafast laser irradiation. *Phys. Rev. B* **2021**, *104*, 104104. [[CrossRef](#)]
24. Bévilion, E.; Stoian, R.; Colombier, J.P. Nonequilibrium optical properties of transition metals upon ultrafast electron heating. *J. Phys. Condens. Matter* **2018**, *30*, 385401. [[CrossRef](#)]
25. Gonze, X.; Amadon, B.; Antonius, G.; Arnardi, F.; Baguet, L.; Beuken, J.M.; Bieder, J.; Bottin, F.; Bouchet, J.; Bousquet, E.; et al. The Abinit project: Impact, environment and recent developments. *Comput. Phys. Commun.* **2020**, *248*, 107042. [[CrossRef](#)]
26. Wales, D.J.; Doye, J.P.K. Global Optimization by Basin-Hopping and the Lowest Energy Structures of Lennard-Jones Clusters Containing up to 110 Atoms. *J. Phys. Chem. A* **1997**, *101*, 5111–5116. [[CrossRef](#)]
27. Vial, A.; Grimault, A.S.; Macías, D.; Barchiesi, D.; de la Chapelle, M.L. Improved analytical fit of gold dispersion: Application to the modeling of extinction spectra with a finite-difference time-domain method. *Phys. Rev. B* **2005**, *71*, 085416. [[CrossRef](#)]
28. Sehmi, H.S.; Langbein, W.; Muljarov, E.A. Optimizing the Drude-Lorentz model for material permittivity: Method, program, and examples for gold, silver, and copper. *Phys. Rev. B* **2017**, *95*, 115444. [[CrossRef](#)]
29. Adachi, S. *The Handbook on Optical Constants of Metals: In Tables and Figures*; World Scientific: Singapore, 2012.
30. Faleev, S.V.; van Schilfgaarde, M.; Kotani, T.; Léonard, F.; Desjarlais, M.P. Finite-temperature quasiparticle self-consistent GW approximation. *Phys. Rev. B* **2006**, *74*, 033101. [[CrossRef](#)]
31. Chang, H.T.; Guggenmos, A.; Cushing, S.K.; Cui, Y.; Din, N.U.; Acharya, S.R.; Porter, I.J.; Kleineberg, U.; Turkowski, V.; Rahman, T.S.; et al. Electron thermalization and relaxation in laser-heated nickel by few-femtosecond core-level transient absorption spectroscopy. *Phys. Rev. B* **2021**, *103*, 064305. [[CrossRef](#)]